Lab on a Chip

COMMUNICATION

View Article Online
View Journal | View Issue

Cite this: *Lab Chip*, 2026, **26**, 1820

Received 9th September 2025,
Accepted 28th January 2026

DOI: 10.1039/d5lc00857c

rsc.li/loc

A smart 3D microfluidic tumor spheroid-vessel co-culture model for studying exosomal HSP-mediated tumor invasion and angiogenesis

Sisi Zhou,†[a] Fanshu Shan,†[b] Yue Zhang,[b] Yu Cao,[b] Junhui Cen,[c] Noritada Kaji [de] and Songqin Liu *[ab]

Breast cancer is one of the most prevalent malignant tumors in women, primarily due to their metastasis and recurrence. Deciphering the molecular mechanisms underlying breast cancer metastasis and recurrence remains a major challenge. Herein, we developed a microfluidic chip-based 3D co-culture system that integrates tumor spheroids, vascular endothelial cells, and extracellular matrix to model metastasis dynamics. This system enables real-time monitoring of tumor invasion and angiogenesis through immunofluorescence staining of zinc finger transcription factor (ZEB1) and platelet–endothelial cell adhesion molecule (CD31), coupled with vascular endothelial growth factor (VEGF) quantification. Then we employed this platform to investigate the role of exosomal hot shock proteins (HSPs) in breast cancer metastasis, elucidating that breast cancer-derived exosomes significantly promoted tumor invasion and angiogenesis in a dose-dependent manner. At an exosome concentration of 10^{12} particles per mL, ZEB1 expression increased by 2.06-fold and VEGF secretion elevated by 3.92-fold. Conversely, HSP-depleted exosomes ($Exosome^{HSP\ del}$) reversed these effects, confirming that exosomal HSPs serve as critical mediators of tumor invasion and angiogenesis. This microfluidic model provides a physiologically relevant tool for studying metastatic mechanisms and screening therapeutic targets, highlighting exosomal HSPs as a promising intervention point.

1. Introduction

Breast cancer is a common malignancy in women, and despite advancements in early diagnosis and treatment,[1,2] metastasis and recurrence remain the leading causes of death.[3–5] Tumor invasion and angiogenesis are key processes in cancer progression, and their mechanism studies are of great significance for the development of cancer treatment strategies. The HSP family, as molecular chaperones, play a central role in protein folding and stress responses.[6,7] Tumor cells overexpress HSP90 and HSP70 to promote invasion and activate signaling pathways such as PI3K/AKT and NF-κB.[8] Elevated HSP expression in breast cancer is associated with poor prognosis.[9] However, studying HSPs is challenging due to their short half-life and instability.[10,11] Exosomes, as extracellular vesicles with diameters ranging from 30 to 150 nm, carry bioactive molecules such as HSPs and miRNAs to mediate intercellular signaling.[12–15] Notably, exosomes protect HSPs from degradation, making them ideal for studying cancer progression.[16]

The invasive growth and angiogenesis of tumors are key processes in the progression of malignant tumors, orchestrated by complex signaling interactions between tumor cells and their microenvironment. Research models for studying breast cancer metastasis are mainly *in vivo* and *in vitro* models.[17–19] Patient-derived xenografts (PDXs) are a classic *in vivo* approach but have limitations like long experimental cycles, high costs, and potential biological relevance issues due to murine stromal cell infiltration into tumors. *In vitro* models are typically 2D or 3D systems. Traditional 2D monolayer cell cultures fail to replicate physiological conditions or the tumor microenvironment accurately.[20] 3D models, cultured in collagen or Matrigel, better maintain the spherical structure of tumors.[21] Patient-derived organoids (PDOs) and patient-derived explant cultures (PDECs) have become innovative tools to study tumor progression.[22] However, these 3D models often lack multicellular interactions and realistic fluid dynamics.

[a] *Analysis and Testing Center, Southeast University, Nanjing 210096, China. E-mail: liusq@seu.edu.cn*
[b] *Jiangsu Engineering Laboratory of Smart Carbon-Rich Materials and Device, School of Chemistry and Chemical Engineering, Southeast University, Nanjing 211189, China*
[c] *School of Materials Science and Engineering, Southeast University, Nanjing 211189, China*
[d] *Department of Applied Chemistry, Graduate School of Engineering, Kyushu University, 744 Motooka, Nishi-ku, Fukuoka 819-0395, Japan*
[e] *Institute of Nano-Life-Systems, Institutes of Innovation for Future Society, Nagoya University, Furo-cho, Chikusa-ku, Nagoya 464-8603, Japan*
† These authors contributed equally to this work.

Advances in microfabrication have led to the development of tumor-on-a-chip systems with complex microstructures. These chips provide physiochemically mimetic microenvironments and intricate tissue architectures with diverse cell types, allowing real-time visualization of tumor dynamics. They show great potential in elucidating tumor metastasis mechanisms and are valuable in research applications.[23–25] Sukanya *et al.* demonstrated the feasibility of real-time 3D tissue-specific invasion of cancer stem-like cells (CSCs) from two primary tumors using a microfluidic device. This chip effectively replicates *in vitro* biochemical conditions for differentiating tissue-specific invasion phenotypes and drug resistance screening.[26] Neto *et al.* proposed a novel suspended spherical droplet system capable of generating independent spheres at high throughput for mimicking *in vivo* tumor models at a laboratory scale.[27] Hence, microfluidic platforms are increasingly used as *in vitro* models to study tumor metastasis, offering a powerful tool to explore breast cancer metastasis mechanisms in depth.[28–31] Nevertheless, current studies predominantly concentrate on static analyses of direct cell-to-cell contact or soluble factors, with limited systematic observations of tumor-derived exosomes and the regulatory functions of key molecules like HSPs in tumor–vascular communication.

Herein, we innovatively constructed a microfluidic-based 3D tumor spheroid-vascular co-culture system, integrating live-cell imaging and molecular interference techniques to dissect the dual roles of exosomal HSPs in tumor invasion and angiogenesis (Fig. 1). The platform precisely controls spatial structures and cell ratios to reconstruct the tumor–vascular interface microenvironment. Additionally, we generated HSP-depleted exosomes (Exosome$^{HSP\ del}$) as a control group to investigate the functional contributions of exosomal HSPs in tumor metastasis. Immunofluorescence staining with zinc finger transcription factor (ZEB1) and platelet–endothelial cell adhesion molecule (CD31) was used to visualize tumor invasion and angiogenesis, respectively. Vascular endothelial growth factor (VEGF) expression was monitored as a supplementary angiogenesis indicator. Overall, this study not only provides new insights into the molecular mechanisms underlying tumor invasion and metastasis but also demonstrates the advantages of microfluidic chips for tumor microenvironment research, paving the way for developing exosomal HSP-targeted anti-cancer therapies.

2. Materials and methods

2.1 Materials and reagents

Polydimethylsiloxane (PDMS) was purchased from Dow Corning (USA). Silicon wafers were obtained from Shanghai Jingxiang Electronic Technology Co. Ltd. (China). The negative photoresist (SU-8 2050) and developer were acquired from Microchem (USA). Photomasks were supplied by Kunshan Kaisheng Electronics Co. Ltd. Dulbecco's modified Eagle medium (DMEM) and Ham's F-12K culture media, trypsin, fetal bovine serum (FBS), the Live/Dead Cell Staining kit (calcein AM/PI assay), cell membrane green fluorescent dye DiO, Human HSP-90 ELISA Detection kit and cell membrane red fluorescent dye DiI were all procured from Nanjing KeyGen Biotech Co. Ltd. (China). Matrix-Gel (standard type, phenol red-free), cy3-labeled goat anti-mouse IgG (H + L), actin-tracker red-555 (red fluorescent β-actin probe), ganetespib, and GW4869 were purchased from

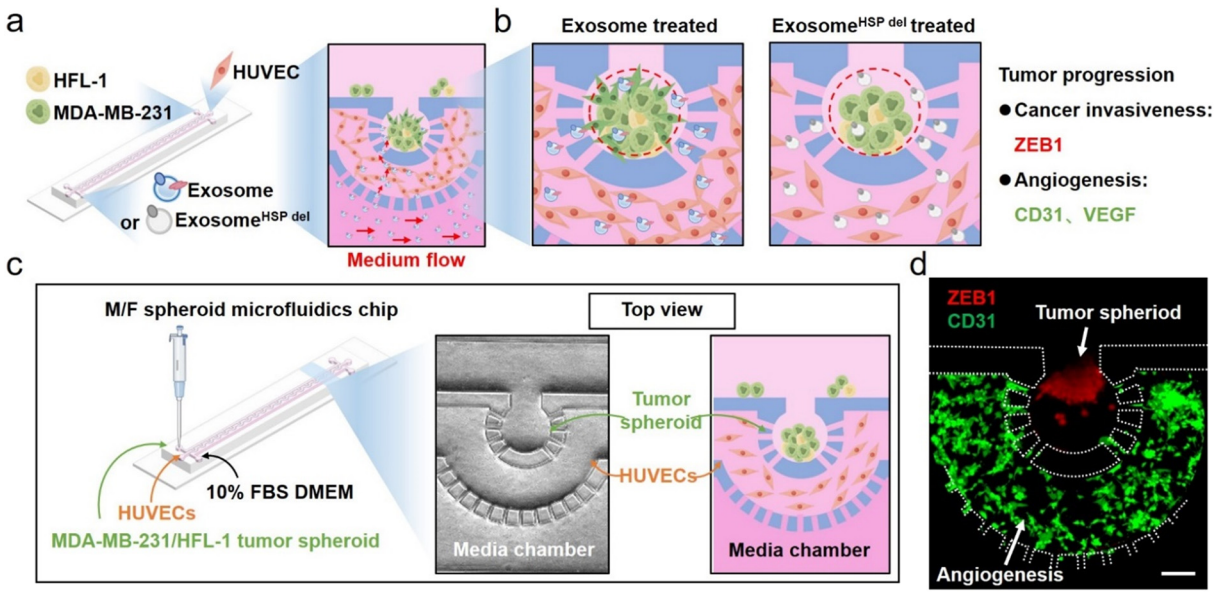

Fig. 1 Schematic diagram of the 3D tumor spheroid-vascular microfluidic chip. (a) Illustration showing co-culture of MDA-MB-231-derived exosomes with on-chip tumor spheroids and HUVECs. (b) Magnified view of chip sections: the left panel shows the exosome-treated group; the right panel shows HSP-inhibited exosome treatment group (Exosome$^{HSP\ del}$ treated). (c) Top view of the 3D tumor spheroid-vascular chip. (d) Fluorescence images of the chip after immunofluorescence staining (scale bar: 150 μm).

Beyotime Biotechnology (China). FITC-labeled CD31 monoclonal antibody was obtained from Thermo Fisher Scientific (USA). ZEB1 monoclonal mouse antibody was sourced from Saining Biotechnology. The VEGF enzyme-linked immunosorbent assay (ELISA) kit was provided by Lianke Biotechnology (China). Ultrapure water (18.2 MΩ cm at 25 °C) used in the experiments was produced by a Thermo Scientific water purification system (USA).

2.2 Cell culture

All cell lines were sourced from the Cell Bank of the Type Culture Collection of the Chinese Academy of Sciences (Shanghai, China). Human breast cancer cells (MDA-MB-231) and HUVECs were cultured in DMEM supplemented with 10% fetal bovine serum (FBS) and 1% antibiotics (100 U mL^{-1} streptomycin and penicillin). Human fetal lung fibroblast-1 (HFL-1) cells were maintained in F12K medium with 10% FBS and 1% antibiotics. All cells were incubated in a 5% CO_2 atmosphere at 37 °C.

2.3 Exosome isolation and characterization

MDA-MB-231 cells were cultured in T175 flasks until ~80% confluent, and the medium was replaced with serum-free DMEM and incubated for 48 h. Then, the medium was harvested and subjected to differential ultracentrifugation: first at 10 000*g* for 60 minutes at 4 °C to remove cells, cellular debris, and large vesicles, followed by ultracentrifugation at 100 000*g* for 70 min at 4 °C to pellet exosomes. Purified exosomes were resuspended in PBS, aliquoted, and stored at −80 °C. Characterization was performed *via* transmission electron microscopy (TEM) and nanoparticle tracking analysis (NTA) using established protocols.[32]

For Exosome$^{HSP\ del}$ preparation, MDA-MB-231 cells were cultured in T175 flasks until reaching 90% confluence, at which point the medium was replaced with the complete medium containing 10% FBS and varying concentrations of ganetespib (HSPs inhibitor). After 24 h of treatment, culture supernatants were collected to isolate exosomes. The expression of exosomal HSPs was assessed *via* western blot (WB).

2.4 Western blot

Cells or exosomes were lysed in RIPA lysis buffer on ice. Then, samples were centrifuged at 12 000 × *g* for 15 min at 4 °C. The supernatant was collected as the total protein extract. Protein concentration was determined using the BCA Protein Assay kit. 20 μg of protein samples were separated on 10% SDS-PAGE gels. Proteins were then transferred onto pre-activated PVDF membranes at 300 mA for 30 min. Membranes were blocked with 5% skim milk at room temperature (RT) for 30 min. Following blocking, membranes were incubated overnight at 4 °C with primary antibodies against GAPDH (1 : 1000) and HSPs (1 : 1000). Membranes were then treated with the secondary antibody (1 : 3000) for 30 min at RT. Chemiluminescent detection was performed, and images were saved as TIFF files.

2.5 Exosome endocytosis assay

Exosomes (10^9 particles per mL) were labeled with 1 μM DiO dye for 15 min in the dark. The mixture was centrifuged at 100 000*g* for 70 min, and the pellet was washed three times with PBS to remove unbound dye. Cells were seeded in confocal dishes, allowed to adhere, and incubated with DiO-labeled exosomes (10^8 particles per mL) in the complete medium for 24 h. After washing with PBS, cells were imaged using to confocal microscopy to visualize exosome uptake.

2.6 Chip fabrication and feasibility verification

The structure and dimensions of the 3D tumor spheroid-vessel co-culture microfluidic chip are shown in Fig. 1. The microfluidic chip comprised 20 independent tumor spheroid-vessel co-culture units, with each unit divided into three functional zones: (a) a semicircular region for tumor spheroid culture, (b) a fan-shaped region for HUVEC growth, and (c) a medium channel. 8 microchannels with a diameter of 20 μm were arranged laterally between the tumor spheroid zone and HUVEC zone, while 12 10 μm-diameter microchannels were set between the HUVEC culture zone and the medium channel (Fig. S1). The height of the channel was 100 μm. The chip was fabricated by standard soft lithography techniques as previous described.[32] Prior to integration, a glass slide substrate and PDMS layer were air plasma-treated for 60 s in a PDC-MG plasma cleaner (Chengdu Mingheng Technology Co. Ltd.). Then the PDMS was promptly aligned onto the glass slide and manually pressed for 10 s to ensure adhesion, followed by thermally cured on a hot plate at 120 °C for 10 min. Subsequently, the chip was dried at 60 °C, and UV-sterilized for 20 min to ensure sterility prior to cell culture.

Leakage testing was conducted by sequentially injecting Matrigel-mixed ink with different colors into the tumor spheroid channel and HUVEC channel, followed by immediate microscopic observation and image acquisition to assess channel integrity. To evaluate the biomolecular diffusion capacity across the microchannels, a 1 : 1 mixture of culture medium and Matrigel was sequentially loaded into both the tumor spheroid channel and HUVEC channel. After gelation, fresh medium containing green fluorescence-labeled secondary antibody (1 : 200 dilution) was introduced into the medium channel. Fluorescence diffusion was recorded at multiple time points using fluorescence microscopy, with intensity quantified using ImageJ software. To assess region-specific cell sedimentation capacity, the cell suspension was injected into the tumor spheroid channel and vertically incubated. Cell settling into microwells was observed and recorded at 5-minute intervals until complete sedimentation was achieved.

2.7 Cell loading and co-culture on the microfluidic chip

The procedure for cell loading into the specified chip region is illustrated in Fig. S2. Firstly, MDA-MB-231 and HFL-1 suspensions were mixed at a 12 : 1 ratio to obtain the M/H dual-cell suspension.[33] The M/H suspension was then combined with Matrigel matrix on ice at a 1 : 1 ratio and gently pipetted to form the M/H cell loading solution. Subsequently, 7 μL of the solution was slowly injected into the sterilized and pre-chilled tumor spheroid channel (Fig. S2-I). After that, the chip was vertically positioned on ice for 15 min to allow cell sedimentation into the circular microwells *via* gravity (Fig. S2-II). Finally, the chip was transferred to the incubator (37 °C, 5% CO_2) and maintained vertically for an additional 20 min to facilitate Matrigel gelation (Fig. S2-III). Secondly, HUVECs were mixed with Matrigel matrix as described above to prepare the HUVEC loading solution. The pre-incubated chip containing the M/H cell solution was retrieved, and 10 μL of the HUVEC solution was slowly injected into the HUVEC channel (Fig. S2-IV). And the chip was returned to the incubator horizontally for 20 min to allow Matrigel gelation (Fig. S2-V). Once cell loading was complete, six matched sterile pipette tips were plugged into the inlets and outlets of the channels as media reservoirs (Fig. S2-VI).[33] the reservoirs at one side channel were filled with the DMEM, while the reservoirs at the other side channel were empty (Fig. S3). The assembled microfluidic chip was placed in a humid box and cultured in a 37 °C and 5% CO_2 cell incubator. The culture medium was refreshed every day. For exosome co-culture experiments, the culture medium is replaced with the exosome-contained medium, and then the exosome-contained medium is loaded using a pipette tip like above. The supernatants were collected every day for the tests of protein production and secretion.

To elucidate on-chip tumor spheroid growth dynamics, MDA-MB-231 and HFL-1 cells were labeled with 5 μM DiO (green) and DiI (red) fluorescent dyes, respectively, prior to preparing the M/H dual-cell suspension. The tumor spheroid formation was monitored at different culture time points using fluorescence microscopy.

To assess on-chip cell viability, the culture medium was supplemented with 5 μg mL^{-1} calcein-AM and propidium iodide (PI). After 30 minutes of incubation in the dark, the staining solution was replaced with PBS. Cell viability was evaluated by confocal microscopy, with viable cells exhibiting green fluorescence (calcein-AM labeling) and dead cells showing red fluorescence (PI staining).

To investigate tumor invasiveness, all cells on the chip were fixed with 4% paraformaldehyde (PFA) for 15 min at RT, permeabilized with 0.25% Triton X-100 for 15 min, and blocked with 5% BSA for 1 h. Subsequently, ZEB1 mouse monoclonal antibody (1 : 100 dilution) in PBS containing 5% BSA and 0.1% Triton X-100 was applied and incubated overnight at 4 °C. Next, the cells were incubated with Cy3-conjugated IgG secondary antibody (1 : 100 dilution) for 30 min at RT in the dark. After washing with PBS, cells in tumor spheroid channel were imaged using fluorescence microscopy, fluorescent colors were inverted to black and white, and the intensities of ZEB1 were measured using the ImageJ software.

To evaluate the formation of HUVEC microvascular networks, cells in the HUVEC region were stained with FITC-conjugated CD31 antibody (1 : 100 dilution) and Actin-Tracker Red-555 (1 : 100 dilution). Besides, VEGF expression levels were analyzed by collecting the conditioned medium from the chip outlet. The samples were subjected to centrifugation at 2000 rpm for 5 min to remove cellular debris and other particulates. The supernatant was harvested and aliquoted for storage at −80 °C until analysis. VEGF concentrations in the collected medium were quantified using a human VEGF ELISA kit in strict adherence to the manufacturer's protocol. All experiments were performed with at least three independent biological replicates to ensure data reproducibility.

3. Results and discussion

3.1 Design and feasibility validation of chip architecture

To investigate the effects of exosomes and Exosome$^{HSP\ del}$ on tumor invasion and angiogenesis, an intelligent microfluidic chip was designed for simultaneous on-chip coculture of 3D tumor spheroids and microvascular networks. Firstly, to ensure that the microfluidic chip architecture effectively supports the co-culture of tumor spheroids and vascular endothelial cells, as well as efficient biomolecular diffusion, the width of channels that physically connect the tumor spheroid and endothelial compartments were optimized. Given the typical cell diameter (10–25 μm), three microchannel widths (10, 20, and 25 μm) were selected. The results demonstrated that larger width facilitated faster molecular diffusion rates, which is beneficial for intercellular signaling. However, when the microchannel width reached 25 μm, cells migrated through the gaps into the opposing channel, resulting in incomplete spheroid structures or positional shifts (Fig. S4). By balancing the constraints of cell confinement with the efficiency of molecular diffusion, 20 μm was subsequently adopted in all following experiments.

As illustrated in Fig. 2a, when M/H cells were perfused into the channels and allowed to settle during 10-minute static incubation on ice, they specifically accumulated at the base of semicircular microchambers with no detectable cell infiltration into the underlying fan-shaped zones. This confirmed the microchannel architecture's ability to restrict cellular movement, thereby maintaining isolated cultivation of individual tumor spheroids. Control experiments with Matrigel-mixed ink with different colors showed no initial cross-channel contamination, though complete chip saturation occurred within 10 minutes (Fig. 2b). Fluorescence tracking experiments revealed progressive biomolecular transport: when fluorescence labeled antibodies were

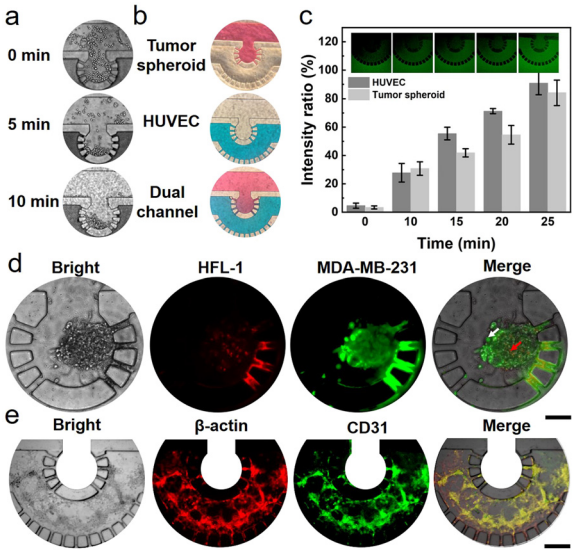

Fig. 2 Chip feasibility validation. (a) Cell sedimentation process. (b) Leakage detection. (c) Molecular diffusion (inset: fluorescence image of tumor spheroids and vascular endothelial cells channels). (d) Characterization of M/H dual-cell tumor spheroids on-chip, scale bar: 100 μm. (e) Characterization of microvascular networks on-chip. Scale bar: 150 μm.

introduced into the medium channel, the initially confined green fluorescence gradually permeated adjacent channels. Quantitative analysis showed that after 25 minutes of diffusion, the fluorescence intensity reached 91% of the source level in HUVEC channels and 85% in tumor spheroid channels, demonstrating efficient inward diffusion of biomolecules from the medium channel (Fig. 2c).

Given that the spatial position of tumor spheroids within microwells significantly affects angiogenesis phenotypes, this study innovatively developed a collaborative positioning strategy. By integrating circular microwell design, gravity-assisted cell sedimentation, and matrix gel encapsulation technology, we achieved precise control and standardization of the spatial position of tumor spheroids. Specifically, 1) the cell suspension is loaded in a vertical chip orientation, utilizing gravity to rapidly sediment cells to the bottom of the microwells, ensuring consistent initial positioning; 2) the geometric constraint effect of circular microwells guides sedimented cells to efficiently aggregate into spheroids within the confined space, reducing morphological variations; 3) the matrix gel is pre-mixed in the microwell channels and induced to gelate at 37 °C, thereby firmly anchoring the tumor spheroids at the predetermined bottom positions of the microwells during conventional horizontal culture, preventing spheroid displacement. Fig. S5 shows that this strategy successfully achieved tumor spheroids at the lower-middle part of the microwells, significantly enhancing the standardization of spheroid positions across different microwells. Thus, this microfluidic chip integrated physical cell confinement with controlled molecular exchange, fully meeting the requirements for sophisticated on-chip cell/tumor spheroid coculture applications.

3.2 Construction of biomimetic tumor spheroid-vessel co-culture model

In 3D *in vitro* culture systems, co-culturing tumor cells with fibroblasts generates tumor spheroids that more accurately mimic the *in vivo* tumor microenvironment compared to homotypic tumor cell spheroids. Fibroblasts play a pivotal role as both structural scaffolds and signaling hubs. They secrete extracellular matrix components that enhance spheroid mechanical integrity and facilitate cell aggregation. Simultaneously, they function as signaling hubs, secreting mitogenic factors to drive proliferation and exerting physical forces to guide invasion.[34,35] Therefore, breast cancer cells (MDA-MB-231) and fibroblasts (HFL-1 cells) were mixed to form tumor spheres. Besides, several critical factors influenced the model construction. Primary optimization focused on cell seeding densities in both cellular channels. In the tumor spheroid zone, the size of the tumor spheroids gradually increased with the increasing of cell density. When the M/F cell density increased to 1×10^5 cells per μL, the tumor spheroid filled almost the entire microchamber with a small amount of cells overflowing. However, a cell density of 5×10^4 cells per μL yielded a single tumor spheroid of 200 μm in diameter with minimal background contamination in the microchamber (Fig. S6a and b). Therefore, 5×10^4 cells per μL of M/F cell density was selected for the construction of tumor spheroids. Fluorescence imaging as shown in Fig. 2d revealed the simultaneous presence of both red and green fluorescence signals, confirming the successful formation of dual-cell tumor spheroids within the microchambers. On the other hand, in the HUVEC culture region, insufficient cell density led to excessive intercellular distances, thereby impeding the formation of functional junctions and subsequent vascular network assembly (Fig. S6c). Conversely, excessive density resulted in HUVEC overcrowding, which significantly inhibited cellular extension. Therefore, 5×10^4 cells per μL was selected as the optimal seeding density that achieved both complete channel coverage and promoted the formation of the characteristic vascular network morphology (Fig. S6c). Quantitative analysis using ImageJ software demonstrated that microvascular networks formed at this optimized density exhibited the highest branch point density (Fig. S6d).

Further characterization was performed using β-actin to evaluate cytoskeletal organization and CD31 (PECAM-1), an established endothelial marker, to assess angiogenic potential.[36] Immunofluorescence analysis revealed that HUVECs formed extensively interconnected networks with elongated cytoskeletal structures (β-actin staining), while CD31 labelling confirmed the development of microvascular networks with the characteristic slender morphology (Fig. 2e). The complete colocalization of β-actin and CD31 signals provided conclusive evidence for the successful establishment of on-chip microvascular networks.

The uniformity of tumor spheroids size in microwells is critical to ensure inter-experimental comparability. Fig. S7

shows that cells within the microwells adhered and grew while maintaining the cluster morphology formed after sedimentation. In the absence of exogenous stimuli, the spheroids remained dimensionally stable over 2 days, with diameters maintained at approximately 200 μm. This provides a highly comparable 3D model system for subsequent research. Besides, the temporal viability profiles of tumor spheroids and HUVECs on the microfluidic chip were quantitatively assessed. This revealed a gradual decline in tumor spheroid viability with prolonged culture duration, yet maintained >60% viability after 72 hours (Fig. S8). Notably, HUVECs exhibited remarkably stable viability, sustaining >95% survival rates throughout the 72-hour culture period (Fig. S9). Thus, both cellular components maintained excellent viability on the microfluidic chip, establishing a reliable foundation for subsequent experimental investigations.

3.3 Effects of exosomes on tumor invasion and angiogenesis

Previous studies have shown that exosomes derived from tumors carry various cargoes (such as proteins and nucleic acids), which regulate the tumor microenvironment through intercellular communication and play a key role in tumor development.[37–40] For instance, exosomes derived from chronic myeloid leukemia cells contain the cytokine TGFβ1, which binds to the TGFβ1 receptor on leukaemia cells, thereby promoting tumor growth by activating ERK, AKT, and anti-apoptotic pathways in the producer cells.[41] Exosomes produced by tumor cells can also modulate endothelial cell properties to promote angiogenesis. Under hypoxic conditions, lung cancer cells produce more exosomes enriched with miR-23a, which targets the tight junction protein ZO1, increasing vascular permeability and cancer migration.[42] Collectively, the diverse cargoes within exosomes collaborate synergistically to amplify and enhance tumor malignancy.

To explore the underlying mechanisms of breast cancer-derived exosomes in metastasis, the medium containing 10 μM gw4869 (an exosome secretion inhibitor) and different concentrations of exosomes (0 ~ 10^{12} particles per mL) was perfused into the medium channel. GW4869 can effectively eliminate the interference of exosomes secreted by cells within the chip. As a master regulator of the epithelial–mesenchymal transition (EMT), ZEB1 promotes tumor invasion and metastasis by repressing epithelial markers such as E-cadherin to disrupt cell adhesion and facilitate cancer cell detachment, while simultaneously inducing mesenchymal markers (including N-cadherin, vimentin, and fibronectin) to drive cytoskeletal reorganization and enhance cellular motility;[43–45] furthermore, functioning as a downstream effector of TGF-β, Wnt/β-catenin, and Notch pathways, ZEB1 amplifies EMT signaling and acts synergistically with β-catenin to reinforce the mesenchymal phenotype. Therefore, the expression of ZEB1 was chosen as a marker for tumor invasion. Following 24-hour incubation,

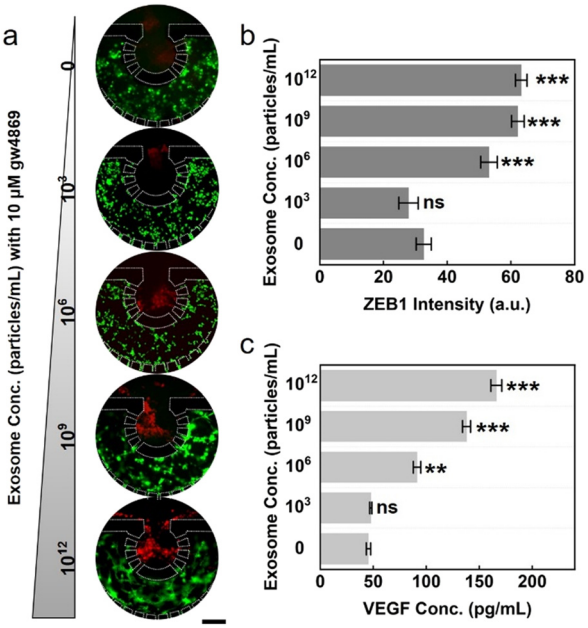

Fig. 3 Effects of MDA-MB-231-derived exosomes on tumor invasion and angiogenesis. (a) Immunofluorescence images after 24-hour on-chip co-culture with different exosome concentrations. Red: ZEB1, green: CD31. Scale bar: 150 μm. (b) Tumor invasion assessment: quantitative analysis of ZEB1 fluorescence intensity. (c) Angiogenesis evaluation: VEGF concentration measured by ELISA. Error bars indicate standard deviations from triplicate experiments. Two-tailed *t*-test, $*p < 0.05$, $**p < 0.01$, $***p < 0.001$, ns = not significant.

the fluorescence intensity of ZEB1 increased in a gradient manner with the increase of exosome concentration. Meanwhile, CD31 staining showed that high concentrations of exosomes (10^9 and 10^{12} particles per mL) significantly promoted the formation of vascular networks in HUVEC channels (Fig. 3a). In addition, the level of VEGF in the culture medium showed a concentration-dependent increase. When the exosome concentration was $\geq 10^6$ particles per mL, both the ZEB1 fluorescence intensity and VEGF concentration showed statistically significant differences compared with the control group (0 particles per mL) (Fig. 3b and c). Time gradient experiments confirmed that after co-culture with 10^{12} particles per mL exosomes, ZEB1 and VEGF continued to increase over time (Fig. S10). Therefore, exosomes derived from highly invasive breast cancer cells can promote tumor invasion and angiogenesis. Moreover, the constructed tumor spheroid-microvascular model on the chip can sensitively respond to microenvironmental heterogeneity and has the potential for application in evaluating the progression of tumor invasion and angiogenesis.

3.4 Construction and characterization of HSP-depleted exosomes (Exosome$^{HSP\ del}$)

Some reports illustrated that HSPs promote neovascular formation by directly stimulating endothelial cell

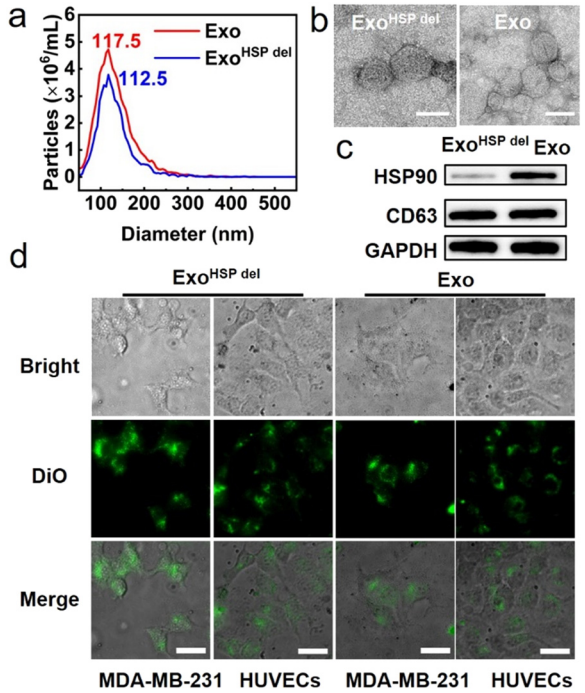

Fig. 4 Characterization of Exosome$^{HSP\ del}$. (a) NTA analysis of exosome and Exosome$^{HSP\ del}$. (b) Western blot analysis of protein composition in the exosomes. (c) TEM images of exosome and Exosome$^{HSP\ del}$ (scale bar: 100 nm). (d) Fluorescence microscopy analysis demonstrating the internalization efficiency of both exosome and Exosome$^{HSP\ del}$ (scale bar: 25 μm).

proliferation and migration through upregulation of VEGF expression.[46] To explore the role of HSP in exosomes in tumor invasion and angiogenesis, HSP-knockdown exosomes (Exosome$^{HSP\ del}$) were prepared by using ganetespib as an HSP inhibitor to treat MDA-MB-231 cells (Fig. S11). NTA testing showed that the mean particle size was 112.5 nm (117.5 nm in the untreated group), and TEM revealed intact phospholipid bilayer structures (Fig. 4a and b). Western blot detection showed that the obtained exosomes retained the expression of the exosomal marker protein CD63 but lacked HSP expression (Fig. 4c). Besides, we quantitatively analyzed the HSP concentration on HSP-depleted exosomes and MDA-MB-231 cell-derived exosomes using an HSP-specific ELISA kit (Fig. S12). The result showed that the HSP content in the HSP-depleted exosomes was significantly reduced (0.26 pg μg^{-1} *vs.* 1.59 pg μg^{-1} (HSP/total proteins of exosomes)), further indicating the successful preparation of HSP-deficient exosomes. Thus, ganetespib treatment did not affect the exosome secretion ability of cells and retained the basic biological characteristics of exosomes. The prepared Exosome$^{HSP\ del}$ were labeled with DiO fluorescent dye and co-cultured with MDA-MB-231 cells and HUVEC cells for 24 hours. Fluorescence microscopy imaging (Fig. 4d) revealed intense green fluorescence signals in the cytoplasmic compartments of both cell types, confirming successful cellular uptake of the exosomes.

3.5 Effects of exosomal HSPs on tumor invasion and angiogenesis

Next, the role of exosomal HSPs in tumor invasion and angiogenesis was further explored. Compared with the complete inhibition group (gw4869 treatment group), the control group (untreated group) showed higher ZEB1 expression, stronger angiogenic ability, and higher VEGF levels, indicating that the exosomes secreted by the cells (especially MDA-MB-231 cells) during the chip culture process also promote tumor invasion and angiogenesis. Therefore, all subsequent exosome treatment groups were supplemented with gw4869 to eliminate this interference effect. The experimental results (Fig. 5) showed that the exosome treatment group derived from breast cancer cells (Exo/gw group, 10^{10} particles per mL exosomes containing HSP~10 pg mL^{-1}) had significantly enhanced tumor invasion ability, more obvious vascular network morphology, and higher VEGF expression levels compared to the HSP-deficient exosome group (Exo$^{HSP\ del}$/gw). The HSP concentration gradient experiment (Fig. S13) indicated that the concentration of HSPs was positively correlated with the degree of tumor invasion/angiogenesis, and the HSP inhibitor ganetespib could significantly inhibit the above effects (Fig. 5a). Notably, at equivalent HSP concentrations (10 pg mL^{-1}), the Exo/gw group exhibited significantly stronger pro-invasive and pro-angiogenic effects compared to free HSPs. The underlying mechanism lies in exosomes acting as natural nanoscale carriers: they not only effectively protect HSPs from protease degradation, substantially enhancing HSP stability and half-life in complex

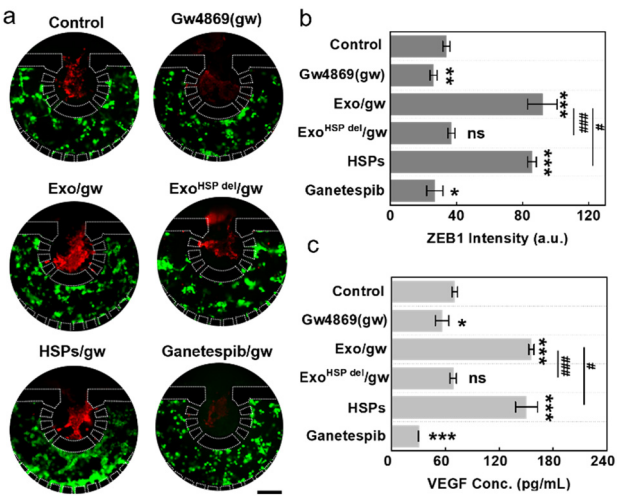

Fig. 5 Effects of HSPs in MDA-MB-231-derived exosomes on tumor invasion and angiogenesis. (a) Immunofluorescence images after 24-hour on-chip co-culture under different treatments. Red: ZEB1, green: CD31. Scale bar: 150 μm. (b) Tumor invasion assessment: quantitative analysis of ZEB1 fluorescence intensity. (c) Angiogenesis evaluation: VEGF concentration measured by ELISA. Exosomes: 10^{10} particles per mL, free HSP: 10 pg mL^{-1}. Error bars indicate standard deviations from triplicate experiments. Two-tailed *t*-test, $^{*/\#}p < 0.05$, $^{**/\#\#}p < 0.01$, $^{***/\#\#\#}p < 0.001$, ns = not significant.

microenvironments, but also mediate efficient recognition and active internalization by target cells, enabling precise intracellular delivery of HSPs. Furthermore, exosome-delivered HSPs form "multimodal signaling complexes" with various synergistic factors (such as miRNAs and proteins), which cooperatively activate key pathways in target cells, generating a signal amplification effect far exceeding that of single free HSPs.[47] Thus, exosomal HSPs are pivotal mediators of tumor metastasis and angiogenesis, representing both a novel target for breast cancer metastasis research and a promising candidate for developing anti-invasion/angiogenesis therapeutics.

4. Conclusions

Exosomes act as "communication messengers" between tumor cells and the microenvironment, transferring HSPs to reprogram recipient cells and synergistically promote tumor invasion and angiogenesis.[46,48] Mechanistically, HSPs induce EMT *via* ZEB1 upregulation (suppressing E-cadherin, promoting vimentin) and remodel the extracellular matrix by activating NF-κB/AKT to induce matrix metalloproteinases (MMPs), enhancing tumor cell motility. Simultaneously, HSPs stabilize VEGFR, and stimulate VEGF secretion to drive angiogenesis (CD31+ vessel formation). This crosstalk was elucidated using a 3D microfluidic tumor–vascular co-culture platform. Compared with other microfluidic models for the tumor spheroid–vascular co-culture, our device employs an innovative segregated co-culture design that significantly outperforms existing mixed culture methods and conventional "upper/lower channel + porous membrane" sandwich structures in both mimicking *in vivo* tumor–vascular interactions and experimental performance. Compared to the mixed culture, the device utilizes microchannels to physically isolate tumor spheroids from endothelial cells. This design effectively overcomes the signal interference caused by direct cell–cell contact in mixed cultures, enabling the independent and precise quantification of exosome-mediated tumor invasion and angiogenesis. Furthermore, the integration of 20 independent units on the chip supports high-throughput screening and avoids the data variability caused by uneven cell distribution inherent in mixed cultures.[33,35] Compared to the conventional sandwich structure, our device cultures cells within parallel microchannels on the same plane. Its core advantage lies in more accurately recapitulating the "parallel distribution" physiological spatial configuration between tumor tissues and blood vessels *in vivo*. In terms of molecular diffusion control, the parallel channels allow molecules to diffuse laterally through the 20 μm side microchannels with minimal resistance. Upon adding stimulatory drugs, molecules achieve efficient diffusion and near-equilibrium status within half an hour (Fig. 2c), establishing a stable and precise concentration gradient. In contrast, the conventional sandwich structure relies on drug penetration through porous membranes, resulting in a tortuous diffusion path, high resistance, and difficulty in achieving a uniform and controllable gradient; moreover, systematic characterization of the diffusion process is rarely reported in related studies.[30,49] Regarding real-time dynamic observation, the device is compatible with confocal microscopy for synchronous imaging. Tumor spheroids (DiO-labeled) and endothelial cells (DiI-labeled) reside within the same focal plane and can be clearly captured simultaneously (Fig. 1d) without frequent refocusing, thereby greatly reducing image registration errors. Conversely, the vertical spatial separation in the sandwich structure requires repeated adjustment of the focal plane, which is prone to introducing time delays and localization deviations. In summary, our innovative microfluidic platform effectively addresses the critical limitations of conventional 2D/3D cell culture models and animal studies by seamlessly integrating real-time monitoring capabilities with high-throughput screening functionality.

In conclusion, our innovative microfluidic platform effectively addresses the critical limitations of conventional 2D/3D cell culture models and animal studies by seamlessly integrating real-time monitoring capabilities with high-throughput screening functionality. Specifically, the platform enables mechanistic discovery and therapeutic screening, demonstrating dose-dependent tumor invasion and angiogenesis mediated by exosomal HSPs. By accurately recapitulating the tumor microenvironment, this model revolutionizes metastasis research, drug efficacy testing, and personalized therapy prediction, while offering scalability for high-throughput applications in precision oncology. Targeting exosomal HSPs disrupts tumor–stromal communication, simultaneously inhibiting invasion and angiogenesis, thereby presenting a dual-action therapeutic strategy that is broadly applicable across cancer types and combinable with existing therapies (*e.g.*, anti-VEGF agents). This integrated engineering–oncology approach not only bridges critical translational gaps but also accelerates the development of targeted therapies for aggressive cancers.

Author contributions

Sisi Zhou: writing (review and editing), supervision, and project administration. Fanshu Shan: original draft, visualization, validation, methodology, and conceptualization. Yue Zhang: formal analysis, investigation, and visualization. Yu Cao: visualization, methodology, and investigation. Junhui Cen: investigation. Noritada Kaji: investigation. Songqin Liu: writing (review and editing), supervision, project administration, and funding acquisition.

Conflicts of interest

There are no conflicts to declare.

Data availability

Supplementary information (SI): Fig. S1 Chip design schematics; Fig. S2 Schematic diagram of the on-chip cell loading process; Fig. S3 Photograph of the medium loaded in the microfluidic chip; Fig. S4 Optimization of the width of channels that physically connect the tumor spheroid and endothelial compartments; Fig. S5 Spatial position of tumor spheroids within different microwells; Fig. S6 On-chip cell density optimization; Fig. S7 Tumor spheres grown on the chip for different periods of time; Fig. S8 Viability assessment of on-chip tumor spheroids; Fig. S9 Viability assessment of on-chip HUVEC cells; Fig. S10 Effects of MDA-MB-231-derived exosomes on tumor invasion and angiogenesis under different incubation times; Fig. S11 Construction of Exosome$^{HSP\ del}$; Fig. S12 The variation trend of Absorbance versus HSP concentration; Fig. S13 Effects of HSPs concentration on tumor invasion and angiogenesis. See DOI: https://doi.org/10.1039/d5lc00857c.

Acknowledgements

This work was supported by the National Natural Science Foundation of China (Grants 22304024 and 22374018).

Notes and references

1 J. Kim, A. Harper, V. McCormack, H. Sung, N. Houssami, E. Morgan, M. Mutebi, G. Garvey, I. Soerjomataram and M. M. Fidler-Benaoudia, *Nat. Med.*, 2025, **31**, 1154–1162.
2 D. Guan, Q. Jie, Y. Wu, Y. Xu, W. Hong and X. Meng, *World J. Surg. Oncol.*, 2022, **20**, 326.
3 V. Padmanaban, I. Krol, Y. Suhail, B. M. Szczerba, N. Aceto, J. S. Bader and A. J. Ewald, *Nature*, 2019, **573**, 439–444.
4 H. Hosseini, M. M. S. Obradovic, M. Hoffmann, K. L. Harper, M. S. Sosa, M. Werner-Klein, L. K. Nanduri, C. Werno, C. Ehrl, M. Maneck, N. Patwary, G. Haunschild, M. Guzvic, C. Reimelt, M. Grauvogl, N. Eichner, F. Weber, A. D. Hartkopf, F.-A. Taran, S. Y. B. Rucker, T. Fehm, B. Rack, S. Buchholz, R. Spang, G. M. Eister, J. A. Aguirre-Ghiso and C. A. Klein, *Nature*, 2016, **540**, 552–558.
5 L. R. Yates, S. Knappskog, D. Wedge, J. H. R. Farmery, S. Gonzalez, I. Martincorena, L. B. Alexandrov, P. Van Loo, H. K. Haugland, P. K. Lilleng, G. Gundem, M. Gerstung, E. Pappaemmanuil, P. Gazinska, S. G. Bhosle, D. Jones, K. Raine, L. Mudie, C. Latimer, E. Sawyer, C. Desmedt, C. Sotiriou, M. R. Stratton, A. M. Sieuwerts, A. G. Lynch, J. W. Martens, A. L. Richardson, A. Tutt, P. E. Lonning and P. J. Campbell, *Cancer Cell*, 2017, **32**, 169–184.
6 W. F. Zuo, Q. Pang, X. Zhu, Q. Q. Yang, Q. Zhao, G. He, B. Han and W. Huang, *J. Hematol. Oncol.*, 2024, **17**, 81.
7 L. Cai, L. Li, X. Chen and L. Jia, *Signal Transduction Targeted Ther.*, 2021, **6**, 276.
8 S. Chatterjee and T. F. Burns, *Int. J. Mol. Sci.*, 2017, **18**, 1978.
9 T. Osada, K. Kaneko, W. R. Gwin, M. A. Morse, A. Hobeika, B. W. Pogue, Z. C. Hartman, P. F. Hughes, T. Haystead and H. K. Lyerly, *Clin. Cancer Res.*, 2017, **23**, 7531–7542.
10 W. Miao, M. Fan, M. Huang, J. J. Li and Y. Wang, *Chem. Res. Toxicol.*, 2019, **32**, 326–332.
11 C. W. Yun, H. J. Kim, J. H. Lim and S. H. Lee, *Cells*, 2020, **9**, 60.
12 R. Isaac, F. C. G. Reis, W. Ying and J. M. Olefsky, *Cell Metab.*, 2021, **33**, 1744–1762.
13 H. M. Nail, C. C. Chiu, C. H. Leung, M. M. M. Ahmed and H. M. D. Wang, *J. Biomed. Sci.*, 2023, **30**, 69.
14 X. Tian, H. Shen, Z. Li, T. Wang and S. Wang, *J. Hematol. Oncol.*, 2019, **12**, 84.
15 C. Zhang, C. Qin, S. Dewanjee, H. Bhattacharya, P. Chakraborty, N. K. Jha, M. Gangopadhyay, S. K. Jha and Q. Liu, *Mol. Cancer*, 2024, **23**, 18.
16 M. Regimbeau, J. Abrey, V. Vautrot, S. Causse, J. Gobbo and C. Garrido, *Semin. Cancer Biol.*, 2022, **86**, 46–57.
17 K. Roarty and G. V. Echeverria, *Front. Oncol.*, 2021, **11**, 645698.
18 T. J. Kwak and E. Lee, *Biofabrication*, 2021, **13**, 015002.
19 X. S. Bittman-Soto, E. S. Thomas, M. E. Ganshert, L. L. Mendez-Santacruz and J. C. Harrell, *Cancers*, 2024, **16**, 1859.
20 P. M. Munne, L. Martikainen, I. Raty, K. Bertula, Nonappa, J. Ruuska, H. Ala Hongisto, A. Peura, B. Hollmann, L. Euro, K. Yavuz, L. Patrikainen, M. Salmela, J. Pokki, M. Kivento, J. Vaananen, T. Suomi, L. Nevalaita, M. Mutka, P. Kovanen, M. Leidenius, T. Meretoja, K. Hukkinen, O. Monni, J. Pouwels, B. Sahu, J. Mattson, H. Joensuu, P. Heikkila, L. L. Elo, C. Metcalfe, M. R. Junttila, O. Ikkala and J. Klefstrom, *Nat. Commun.*, 2021, **12**, 6967.
21 L. Liu, L. Yu, Z. Li, W. Li and W. Huang, *J. Transl. Med.*, 2021, **19**, 40.
22 Z. Dantes, L. Huang, J. Slawska, A. Manjunath, S. Zormaier, L. Ferreira, A. Steininger, F. Mandlmeier, K. Steiger, N. Pfarr, M. Kiechle, R. Rosell, M. Dantes, K. Lindner, W. Weichert, C. Peschel and S. Paepke, *J. Clin. Oncol.*, 2023, **41**, e13594.
23 J. F. Gil, C. S. Moura, V. Silverio, G. Goncalves and H. A. Santos, *Adv. Mater.*, 2023, **35**, 2300692.
24 R. Portillo Lara and N. Annabi, *Lab Chip*, 2016, **16**, 4063–4081.
25 S. Nagaraju, T. Danh, G. Mouneimne and M. Nikkhah, *Adv. Healthcare Mater.*, 2018, **7**, 1701257.
26 V. S. Sukanya, V. Mehta, S. Jilla and S. N. Rath, *Chem. Eng. J.*, 2024, **489**, 151202.
27 A. I. Neto, C. R. Correia, M. B. Oliveira, M. I. Rial-Hermida, C. Alvarez-Lorenzo, R. L. Reis and J. F. Mano, *Biomater. Sci.*, 2015, **3**, 581–585.
28 Y. Wu, Y. Zhou, R. Paul, X. Qin, K. Islam and Y. Liu, *Anal. Chem.*, 2022, **94**, 12159–12166.
29 B. F. L. Lai, R. X. Z. Lu, Y. Hu, L. D. Huyer, W. Dou, E. Y. Wang, N. Radulovich, M. S. Tsao, Y. Sun and M. Radisic, *Adv. Funct. Mater.*, 2020, **30**, 2000545.
30 J. Ro, J. Kim, J. Park, Y. Choi and Y.-K. Cho, *Adv. Sci.*, 2025, **12**, 2410659.
31 M. Humayun, J. M. Ayuso, R. A. Brenneke, M. Virumbrales-Munoz, K. Lugo-Cintron, S. Kerr, S. M. Ponik and D. J. Beebe, *Biomaterials*, 2021, **270**, 120640.
32 S. Zhou, T. Hu, F. Zhang, D. Tang, D. Li, J. Cao, W. Wei, Y. Wu and S. Liu, *Anal. Chem.*, 2020, **92**, 1574–1581.

33 C. Li, S. Li, K. Du, P. Li, B. Qiu and W. Ding, *ACS Appl. Mater. Interfaces*, 2021, **13**, 19768–19777.
34 I. Flörkemeier, L. K. Antons, J. P. Weimer, N. Hedemann, C. Rogmans, S. Krüger, R. Scherliess, A. Dempfle, N. Arnold, N. Maass and D. O. Bauerschlag, *Sci. Rep.*, 2024, **14**, 23526.
35 Z. Wan, M. A. Floryan, M. F. Coughlin, S. Zhang, A. X. Zhong, S. E. Shelton, X. Wang, C. Xu, D. A. Barbie and R. D. Kamm, *Adv. Healthcare Mater.*, 2022, **12**, 2201784.
36 G. Cao, M. L. Fehrenbach, J. T. Williams, J. M. Finklestein, J. X. Zhu and H. M. DeLisser, *Am. J. Pathol.*, 2009, **175**, 903–915.
37 K. Liu, R. Dou, C. Yang, Z. Di, D. Shi, C. Zhang, J. Song, Y. Fang, S. Huang, Z. Xiang, W. Zhang, S. Wang and B. Xiong, *Carcinogenesis*, 2023, **44**, 356–367.
38 A. Garcia-Hernandez, E. Reyes-Uribe, C. Arce-Salinas, K.-G. de la Cruz-Lopez, J. Manzo-Merino, A.-L. Guzman-Ortiz, H. Quezada, P. Cortes-Reynosa, F. Breton-Mora, I. Elizalde-Acosta, R. Thompson-Bonilla and E. Perez Salazar, *Tissue Cell*, 2022, **76**, 101814.
39 S. S. Yang, S. Ma, H. Dou, F. Liu, S. Y. Zhang, C. Jiang, M. Xiao and Y. X. Huang, *Exp. Cell Res.*, 2020, **391**, 111983.
40 X. Qin and Y. Cao, *J. Immunol. Res.*, 2022, 66032076.
41 S. Raimondo, L. Saieva, C. Corrado, S. Fontana, A. Flugy, A. Rizzo, G. De Leo and R. Alessandro, *Cell Commun. Signaling*, 2015, **13**, 8.
42 Y. L. Hsu, J. Y. Hung, W. A. Chang, Y. S. Lin, Y. C. Pan, P. H. Tsai, C. Y. Wu and P. L. Kuo, *Oncogene*, 2017, **36**, 4929–4942.
43 B. C. Roy, T. Kohno, R. Iwakawa, T. Moriguchi, T. Kiyono, K. Morishita, M. Sanchez-Cespedes, T. Akiyama and J. Yokota, *Lung Cancer*, 2010, **70**, 136–145.
44 V. Odero-Marah, O. Hawsawi, V. Henderson and J. Sweeney, *Cell & Molecular Biology of Prostate Cancer: Updates, Insights and New Frontiers*, 2018, vol. 1095, pp. 101–110.
45 L. Wei, T. T. Liu, H. H. Wang, H. M. Hong, A. L. Yu, H. P. Feng and W. W. Chang, *Breast Cancer Res.*, 2011, **13**, R101.
46 K. C. Rashmi, H. S. Atreya, M. H. Raj, B. P. Salimath and H. S. Aparna, *Cell Stress Chaperones*, 2017, **22**, 751–766.
47 S. C. Tao and S. C. Guo, *Cell Commun. Signaling*, 2020, **18**, 163.
48 C. W. Yun, H. J. Kim, J. H. Lim and S. H. Lee, *Cells*, 2020, **9**, 60.
49 J. Bang, J. Yeo, S. J. Lee, H. Lee, J. Kim, S. Jeong, E. Kang, H. S. Rho, Y. Kim and J.-O. Park, *Biomed. Microdevices*, 2025, **27**, 25.